

**Centre for Green Energy and Vehicle Innovation  
Faculty of Engineering and Information Technology  
Centre for Clean Energy Technology  
Faculty of Science**

**Graphene and Metal Oxide Nanomaterials  
for High-performance Supercapacitors**

**A Thesis Presented in Fulfillment of the Requirement for the**

**Degree of**

**Doctor of Philosophy**

**By**

**Yiying Wei, B. E.**

**University of Technology Sydney**

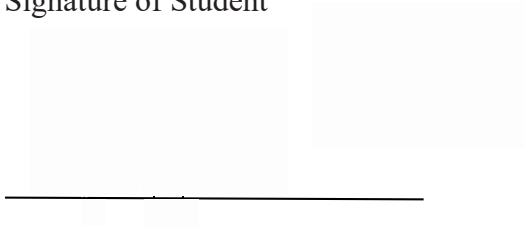
**August 2015**

## **CERTIFICATE OF ORIGINAL AUTHORSHIP**

I certify that the work in this thesis has not previously been submitted for a degree nor has been submitted as part of requirements for a degree except as fully acknowledged within the text.

I also certify that the thesis has been written by me. Any help that I have received in my research work and the preparation of the thesis itself has been acknowledged. In addition, I certify that all information sources and literature used are indicated in the thesis.

Signature of Student



---

August 2015

## ACKNOWLEDGEMENTS

First, I would like to express my sincere gratitude to my supervisors, Prof. Jianguo Zhu and Prof. Guoxiu Wang, who have been guiding and supporting me wholeheartedly through rigorous but fruitful supervision and financial funding for over four years since I started my research career in 2011. Dr. Jane Yao is also gratefully acknowledged for all the administrative assistance and lab management. Thanks are also due to Laurence Stonard, the manager of UTS workshop, who helped me fabricate all the devices I designed.

Special thanks are given to all my colleagues in the research team at the Centre for Green Energy and Vehicle Innovation and Centre for Clean Energy Technology for all the valuable discussions, kind co-operation and assistance. It is a pleasure to have worked with all of you and I really appreciate everyone's efforts in creating an intimate atmosphere for the research work.

I am also grateful for the assistance and patience of A/Prof. Youguang Guo and Dr. Zhiwei Lin, who always gave me the advice and discussion about the technic issues. Relevant training in the research facilities from Dr. Ronald Shimmon, Dr. Linda Xiao, and all the MAU staff are much appreciated as well.

Deep gratitude is to be expressed to my parents and my relatives, who have been caring and sustaining me over these years. Without your continuous support, I could not have finalized my PhD study and become a mature and responsible person.

## LIST OF PUBLICATION

1. **Yiyang Wei**, Bing Sun, Dawei Su, Jianguo Zhu and Guoxiu Wang. "3D Free-Standing NiCo<sub>2</sub>O<sub>4</sub>@graphene Foam for High-performance Supercapacitors." *Advanced Functional Materials*, submitted, 2015. (Impact factor: 11.8)
2. **Yiyang Wei**, Shuangqiang Chen, Dawei Su, Bing Sun, Jianguo Zhu, and Guoxiu Wang. "3D mesoporous hybrid NiCo<sub>2</sub>O<sub>4</sub>@graphene nanoarchitectures as electrode materials for supercapacitors with enhanced performances." *Journal of Materials Chemistry A* 2, no. 21 (2014): 8103-8109. (Impact factor: 7.4)
3. **Yiyang Wei**, Jianguo Zhu, and Guoxiu Wang. "High-Specific-Capacitance Supercapacitor Based on Vanadium Oxide Nanoribbon." (2014). *Applied Superconductivity, IEEE Transactions on*, 2014, 24, (5), 1-4. (Impact factor: 1.2)
4. **Yiyang Wei**, Guoxiu Wang, Jianguo Zhu, "Synthesis and Characterization of Vanadium Oxide Nanotubes as Electrode Materials for Electrochemical Capacitors", *ECS Transactions* 58 (2014) 61-67.
5. **Yiyang Wei**, Shuangqiang Chen, Jianguo Zhu and Guoxiu Wang, "Synthesis and Characterization of Nanoporous NaMn<sub>2</sub>O<sub>4</sub> electrode Material for Sodium-Ion Battery", 17th International Meeting on Lithium Batteries in Como, Italy, June 10 to 14, 2014.
6. Chen, Shuangqiang, Yufei Zhao, Bing Sun, Zhimin Ao, Xiuqiang Xie, **Yiyang Wei**, and Guoxiu Wang. "Microwave-assisted synthesis of mesoporous Co<sub>3</sub>O<sub>4</sub> nanoflakes for applications in lithium ion batteries and oxygen evolution reactions." *ACS applied materials & interfaces* 7, no. 5 (2015): 3306-3313. (Impact factor: 6.7)

## **RECEIVED AWARDS**

2015 UTS FEIT HDR Publications Award

2014 UTS FEIT HDR Publications Award

# TABLE OF CONTENTS

CERTIFICATE OF ORIGINAL AUTHORSHIP.....	I
ACKNOWLEDGEMENTS.....	II
LIST OF PUBLICATION.....	III
RECEIVED AWARDS.....	IV
TABLE OF CONTENTS.....	V
LIST OF SYMBOLS AND ABBREVIATIONS.....	VIII
LIST OF FIGURES.....	X
LIST OF TABLES.....	XXI
ABSTRACT.....	XXII
Chapter 1. INTRODUCTION.....	1
1.1. Research Aims and Objectives.....	1
1.2. Background and Significance.....	2
1.3. Thesis Outline.....	9
Chapter 2. Literature Review.....	11
2.1. Energy Storage Technologies.....	11
2.1.1. Supercapacitors.....	11
2.1.2. Battery.....	15
2.1.3. Flywheel.....	19
2.1.4. Superconductive Magnetic Energy Storage.....	21
2.2. Supercapacitor Metrics and Parameters.....	21
2.2.1. Electrode Surface Area.....	22
2.2.2. Electrode Area-specific Capacitance.....	22
2.2.3. Gravimetric Capacitance of Carbon Electrode.....	22
2.2.4. Volumetric Specific Capacitance.....	22
2.2.5. Impedance.....	23
2.2.6. Power Density.....	23
2.2.7. Energy Density.....	23
2.3. Supercapacitor Modelling.....	23
2.3.1. Physical Model.....	23
2.3.2. Mathematic Model.....	29
2.3.3. Pore Impedance Model.....	32

2.3.4.	Circuit Model with Pore Impedance Model.....	35
2.4.	Electrode materials for supercapacitor .....	41
2.4.1.	Carbon nanotube .....	41
2.4.2.	Graphene-based electrode .....	47
2.4.3.	Unzipped CNTs.....	60
2.4.4.	Vanadium Oxide.....	64
2.5.	Summary .....	71
Chapter 3.	Experimental Methods.....	77
3.1.	Materials synthesis .....	77
3.1.1.	Hydrothermal method .....	77
3.1.2.	Freeze drying.....	81
3.1.3.	Vacuum filtration .....	86
3.1.4.	<i>In-situ</i> self-assembly.....	89
3.2.	Physical and morphological characterization .....	91
3.2.1.	X-ray Diffractometry (XRD) .....	91
3.2.2.	Scanning electron microscopy (SEM).....	92
3.2.3.	Transmission Electron Microscopy (TEM).....	93
3.2.4.	Thermogravimetric Analysis (TGA) .....	94
3.2.5.	Brunauer-Emmett-Teller (BET) Surface Area and Barrett-Joyner-Halenda (BJH) Pore Size and Volume Analysis .....	94
3.3.	Electrode fabrication and electrochemical characterization.....	95
3.3.1.	Electrode fabrication.....	95
3.3.2.	Electrochemical testing.....	96
3.3.2.1.	Cyclic voltammetry (CV).....	96
3.3.2.2.	Galvanostatic Charge/Discharge (DC).....	97
3.3.2.3.	Electrochemical Impedance Spectroscopy .....	98
3.4.	Summary .....	98
Chapter 4.	Synthesis and Characterization of Vanadium Oxide Nanotubes as Electrode Materials for Electrochemical Capacitors.....	99
4.1.	Introduction .....	99
4.2.	Experimental .....	100
4.3.	Results and discussion .....	102
4.4.	Summary .....	106

Chapter 5. High-Specific-Capacitance Supercapacitor Based on Vanadium Oxide Nanoribbon	107
5.1. Introduction .....	107
5.2. Experimental .....	109
5.3. Results and discussion .....	111
5.4. Summary .....	115
Chapter 6. 3D Mesoporous Hybrid NiCo <sub>2</sub> O <sub>4</sub> @graphene Nanoarchitectures as Electrode Materials for Supercapacitors with Enhanced Performances .....	117
6.1. Introduction .....	117
6.2. Experimental .....	119
6.2.1. Fabrication of graphene – polyurethane (PU) sponges .....	119
6.2.2. Preparation of NiCo <sub>2</sub> O <sub>4</sub> @graphene nanoarchitectures .....	119
6.2.3. Materials characterization .....	120
6.2.4. Electrochemical testing.....	120
6.3. Results and Discussion .....	121
6.4. Summary .....	132
Chapter 7. A High-Rigid Binder-Free 3D Free-Standing NiCo <sub>2</sub> O <sub>4</sub> @graphene Foam Fabricated by Controllable Freeze Casting for High-performance Supercapacitors .....	134
7.1. Introduction .....	134
7.2. Experimental .....	139
7.2.1. Fabrication of 3D NiCo <sub>2</sub> O <sub>4</sub> @graphene Precursor .....	139
7.2.2. Fabrication of 3D NiCo <sub>2</sub> O <sub>4</sub> @graphene Foam .....	139
7.2.3. Material Characterization .....	140
7.2.4. Electrochemical testing.....	140
7.3. Results and Discussion .....	141
7.4. Summary .....	157
Chapter 8. Conclusion and Future Work .....	159
8.1. General Conclusion .....	159
8.2. Future Work.....	161
REFERENCES .....	163



## LIST OF SYMBOLS AND ABBREVIATIONS

Abbreviation	Full name
1D	One-dimensional
3D	Three Dimension
ALD	Atomic layer deposition
BET	Brunauer–Emmett–Teller
CAES	Compressed air energy storage
CFC	Controllable freeze casting
CMG	Chemically modified graphene
CNHs	Carbon nanohorns
CNTs	Carbon nanotubes
CPE	Constant phase element
DLCs	Double layer capacitors
EDLCs	Electrochemical double layer capacitors
ESR	Equivalent series resistance
ESSs	Energy storage systems
EVs	Electric vehicles
FES	Flywheel energy storage
FESEM	Field-emission scanning electron microscopy
GONPs	Graphene oxide nanoplatelets
HEVs	Hybrid electric vehicles
ICE	Internal combustion engine
LPCVD	Low-pressure chemical vapor deposition
MWNTs	Multi-walled carbon nanotubes
OHP	Outer Helmholtz Plane
PEI	polyethyleneimine
PHEVs	Plug-in hybrid electric vehicles
PVDC	Ploy vinylidene chloride
SEM	Scanning electron microscopy
SMES	Superconductive magnetic energy storage
SWNTs	Single-walled nanotubes

TEM	Transmission electron microscopy
TMAOH	Tetramethyl ammonium
VN	Vanadium nitride

## LIST OF FIGURES

Figure 2-1 The schematic of the electrolytic capacitor designed by Becker and Ferry. <sup>100</sup> .....	12
Figure 2-2 The schematic of the electrolytic capacitor designed by SOHIO. <sup>101</sup> .....	12
Figure 2-3 Section view of the positive plate. <sup>104</sup> .....	17
Figure 2-4 Helmholtz model. <sup>105</sup> .....	24
Figure 2-5 Potential distribution of Helmholtz model, Gouy-Chapman model and Stern model. <sup>106</sup> .....	25
Figure 2-6 Grahame model and the charge distribution. <sup>108</sup> .....	28
Figure 2-7 Bockris, Devanathan and Muller Model: Water dipole model of the double layer at an electrode/electrolyte interface. <sup>109</sup> .....	28
Figure 2-8 RC network model .....	29
Figure 2-9 The results of experiment and simulation of RC model. <sup>111</sup> .....	30
Figure 2-10 Three RC branches with a voltage-dependent capacitor. <sup>111</sup> .....	31
Figure 2-11 The parameters D. A. New's supercapacitor model. <sup>112</sup> .....	31
Figure 2-12 Equivalent circuit of a pore. <sup>114</sup> .....	32
Figure 2-13 An infinitesimally small section $d_z$ of a pore. <sup>114</sup> .....	33
Figure 2-14 Equivalent circuit of a supercapacitor. <sup>118</sup> .....	35
Figure 2-15 The experimental impedance spectrum and the simulation of standard impedance and generalized impedance model.....	37
Figure 2-16 RC network model. ....	37
Figure 2-17 RC equivalent circuit of ZARC element. <sup>121</sup> .....	38
Figure 2-18 RC parameter of the equivalent circuit of ZARC. <sup>113</sup> .....	38
Figure 2-19 Generalized pore impedance model is represented by a parallel RC circuit	

with the standard pore impedance. <sup>122</sup> .....	39
Figure 2-20 Equivalent impedance model of porous electrode. <sup>118</sup> .....	40
Figure 2-21 Equivalent circuit of ZARC element. <sup>118</sup> .....	40
Figure 2-22 Schematic diagram of the collapse of the aligned low-density as-grown forest (above) to the highly densely packed SWNT solid (below). <sup>58</sup> .....	43
Figure 2-23 SEM image of the aligned CNT. <sup>35</sup> .....	45
Figure 2-24 Comparison of different carbon materials as electrodes of supercapacitors. (a) Activated carbon. Activated carbon has a high surface area. However, many of the micropores cannot be accessed by electrolyte ions. (b) Single-walled carbon nanotube (SWCNT) bundles. SWCNTs usually form bundles, limiting their surface area. Only the outmost surface can be accessed by electrolyte ions. (c) Pristine graphene. Graphene nano-sheets are likely to agglomerate through van der Waals interactions during the drying process. It would be difficult for electrolyte ions to access the ultras-small pores, especially for larger ions such as an organic electrolyte or at a high charging rate. (d) Graphene/CNT composite. SWCNTs can serve as a spacer between the graphene nano-sheets to give rise to rapid diffusion pathways for the electrolyte ions. Moreover, they can enhance electrical conduction for the electrons. The CNTs also serve as a binder to hold the graphene nano-sheets together preventing disintegration of the graphene structure into the electrolyte. <sup>64</sup> .....	48
Figure 2-25 Scheme for preparing (a) reducedGO electrode and (b) GS-CNTs-9-1 electrode. Note the schematic models of GS-CNT composites with various GS/CNTs ratios; where (c) GO are dispersed in the solution and GS aggregates/stacks are formed after reduction, (d) GO and CNTs coexist in the solution and CNTs act as nanospacers to increase the interlayer space between GS after reduction, avoiding the aggregation issue, (e) excess CNTs attach on the surface of GS resulting in a low exposure of surface area,	

and (f) CNTs are dispersed in the solution and CNTs aggregates are formed in the dry state. <sup>125</sup> .....	49
Figure 2-26 Illustration of positively charged PEI-GN and negatively charged MWNT film deposition process on an appropriate substrate. ....	50
Figure 2-27 Scheme representation of the preparation of self-assembled hierarchical nanostructure comprising graphene and carbon spheres. <sup>126</sup> .....	52
Figure 2-28 Cyclic voltammograms (CVs) of supercapacitors constructed with different materials based electrodes in 6MKOH (scan rate of 20 mV s <sup>-1</sup> , electrode mass of 8.2 mg). <sup>126</sup> .....	52
Figure 2-29 Illustration of the electrochemical synthesis process of the PPy/GR nanoplatelet electrodes. ....	53
Figure 2-30 Fabrication of an RG-O and aminated MWNT (RG-O/MWNT) double layer on a substrate. <sup>129</sup> .....	53
Figure 2-31 Fabrication of hybrid suspensions of CCG and CNTs. <sup>69</sup> .....	55
Figure 2-32 Schematic representation of hybrid LbL multilayer of MWNTs and RGO. <sup>130</sup> .....	56
Figure 2-33 Schematic for the assembly of the CNTs/G composite film. <sup>131</sup> .....	57
Figure 2-34 Schematic depiction for the performance comparison of the conventional stacked geometry (a,b) Vs the „in-plane“ geometry (c,d). <sup>133</sup> .....	58
Figure 2-35 Schematic illustration of the fabrication process for carbon hybrid films. <sup>134</sup> .....	59
Figure 2-36 (a) Representation of the gradual unzipping of one wall of a carbon nanotube to form a nanoribbon. Oxygenated sites are not shown. (b) The proposed chemical mechanism of nanotube unzipping. <sup>136</sup> .....	61
Figure 2-37 (a) A pristine MWCNT was used as the starting raw material. (b) The	

MWCNT was deposited on a Si substrate and then coated with a PMMA film. (c) The PMMA–MWCNT film was peeled from the Si substrate, turned over and then exposed to an Ar plasma. (d–g) Several possible products were generated after etching for different times: GNRs with CNT cores were obtained after etching for a short time  $t_1$  (d); tri-, bi- and single-layer GNRs were produced after etching for times  $t_2$ ,  $t_3$  and  $t_4$ , respectively ( $t_4$ ,  $t_3$ ,  $t_2$ ,  $t_1$ ; e–g). (h) The PMMA was removed to release the GNR. .... 63

Figure 2-38 Mmechanism for intercalation and unwrapping of MWNT..... 64

Figure 2-39 Schematic diagram of horizontal alumina tube furnace for growth of vanadium oxides.<sup>143</sup> ..... 66

Figure 2-40 Schematic representation of VN/CNTs nanocomposite synthesis process.<sup>150</sup> ..... 69

Figure 2-41 SEM images of (a) uncoated samples, and samples coated with VOx for (b) 100 ALD cycles, (c) 300 ALD cycles, and (d) 500 ALD cycles.<sup>71</sup> ..... 70

Figure 2-42 Cross-section SEM images of ordered nanotube arrays on different substrates: (a) Ti, (b) Ti<sub>0.2</sub>V, (c) Ti<sub>3</sub>V, and (d) Ti<sub>18</sub>V by anodization in an electrolyte composed of ethylene glycol with 0.2 M HF at 120 V for 30 minutes. (e) and (f) High magnification cross-section and top-view SEM images of the Ti<sub>18</sub>V Ti–V oxide nanotubes.<sup>80</sup> ..... 71

Figure 2-43 An ideal design of the electrode material for next generation supercapacitors, RuO<sub>2</sub>·xH<sub>2</sub>O nanotubular arrayed electrode. The mesoporous architecture, hydrous nature, and metallic conductivity provide the proton and electron “superhighways” for the extremely rapid charge/discharge processes.<sup>74</sup> ..... 72

Figure 2-44 The scheme represents the enhanced charge storage process of the prepared electrode.<sup>156</sup> ..... 73

Figure 2-45 (a) Schematic illustration showing conductive wrapping of graphene/MnO<sub>2</sub> to introduce an additional electron transport path (in a discharge cycle). (b) Schematic of

graphene/MnO <sub>2</sub> /CNT and graphene/MnO <sub>2</sub> /conducting polymer systems formed by wrapping of GM nanostructures with CNTs or conducting polymers (black, graphene; rose, MnO <sub>2</sub> ; yellow, CNTs; blue, conducting polymer). <sup>82</sup> .....	75
Figure 2-46 Structural characterization of MnO <sub>2</sub> /Zn <sub>2</sub> SnO <sub>4</sub> / carbon microfibers hybrid composite. (a-d) SEM images of Zn <sub>2</sub> SnO <sub>4</sub> nanowires grown radially on the woven carbon microfibers. <sup>165</sup> .....	76
Figure 3-1 Typical FESEM images of (A, B) bare carbon nanofibers after Te nanowire core removal; (C, D) NiCo-precursor nanorod arrays/ carbon nanofibers hybrid nanostructure; and (E, F) crystalline NiCo <sub>2</sub> O <sub>4</sub> nanorod arrays/carbon nanofibers hybrid structure obtained by annealing the NiCo-precursor nanorods/carbon nanofibers at 300 °C for 2 h with a slow heating rate of 0.5 °C min <sup>-1</sup> . <sup>89</sup> .....	80
Figure 3-2 Benchtop Manifold Freeze-Dryer marketed by Millrock Technology.....	81
Figure 3-3 The three phase diagram of water.....	82
Figure 3-4 (a-c) Typical top-view (a,b) and side-view (c) SEM images of graphene monolith of 5.10 mg cm <sup>-3</sup> . (d) Schematic showing the formation mechanism of the cork-like monolith by freeze casting. When a well-dispersed pr-GO dispersion (the first scheme) is frozen, pr-GO sheets are concentrated at the boundary of ice crystals and then aligned along the growth direction of ice due to the squeezing effect (the second scheme, side-view). As a result, a continuous honeycomb-like network is formed. The network retains its connectivity when the ice is thawed (the third scheme, top-view). The pr-GO sheets are illustrated as slightly corrugated lines in the scheme with the brown representing partially reduced, whereas the black for fully reduced. Photos of the corresponding samples are presented in the insets. Scale bars, 50 mm (a,c) and 10 mm (b). <sup>156</sup> .....	83
Figure 3-5 (a) Illustration of the fabrication process of the ultralight graphene aerogel (ULGA). (b) Digital images of time-dependent formation process of functionalized	

graphene hydrogel (FGH). <sup>157</sup> .....	85
Figure 3-6 Diagram of vacuum filtration.....	87
Figure 3-7 Low and high magnification SEM images of (a) and (b) mechanically densified aMEGO and (c) and (d) aligned aMEGO. <sup>164</sup> .....	88
Figure 3-8 Schematic drawings illustrating the leavening process to prepare rGO foams. <sup>166</sup> .....	88
Figure 3-9 The proposed self-assembly mechanism for graphene hydrogel formation during the chemical reduction of GO in an aqueous suspension. <sup>167</sup> .....	89
Figure 3-10 Schematic illustrations of the ternary self-assembly approach to ordered metal oxide graphene nanocomposites. <sup>168</sup> .....	90
Figure 3-11 An X-ray diffractometer (Siemens D5000 model) in UTS.....	91
Figure 3-12 An FE-SEM facility (Zeiss Supra 55VP) in UTS. ....	92
Figure 3-13 A commercial TEM setup (JEOL 2011 model).....	93
Figure 3-14 A TGA/DTA Analyzer (SDT 2960 model, TA Instruments) in UTS.....	94
Figure 3-15 A TriStar II Surface Area Analyzer.....	95
Figure 3-16 An electrochemistry workstation (CHI660D model). ....	97
Figure 4-1 XRD pattern of the as-prepared nanotube with the standard V <sub>2</sub> O <sub>5</sub> pattern, (b) Schematic depiction of the nanoribbon structure.....	102
Figure 4-2 The uniform vanadium oxide nanotubes was demonstrated by SEM images (a and b); The detailed information about the nanotubes were shown in the TEM images (c-e).....	103
Figure 4-3 Cyclic voltametric curves of the vanadium oxide nanotubes (a) in 2 M KCl, (b) in 2 M LiCl and (c) in 2 M NaCl at the scan rates of 2 mV s <sup>-1</sup> , 5 mV s <sup>-1</sup> , 10 mV s <sup>-1</sup> , 20 mV s <sup>-1</sup> , and 50 mV s <sup>-1</sup> . (d) Comparison of CV curves in 2 M KCl, 2 M LiCl and 2 M NaCl at the scan rate of 50 mV s <sup>-1</sup> .....	104



Figure 4-4 Measured capacitance of vanadium oxide nanotubes in 2 M KCl, 2 M LiCl and 2 M NaCl at the scan rates of 2 mV s <sup>-1</sup> , 5 mV s <sup>-1</sup> , 10 mV s <sup>-1</sup> , 20 mV s <sup>-1</sup> , and 50 mV s <sup>-1</sup> . .....	106
Figure 5-1 (a) XRD pattern of the as-prepared nanoribbon with the standard V <sub>2</sub> O <sub>5</sub> pattern, (b) Schematic depiction of the nanoribbon structure. ....	111
Figure 5-2 (a) SEM images of nanoribbon, (b, c) low- and high-magnification TEM images, respectively. (d) selected area electron diffraction (SAED). ....	112
Figure 5-3 Cyclic voltametric curves of the vanadium oxide nanoribbon (a) in 2M KCl (b) in 2M NaCl, nanotube at the scan rates of 2 mV s <sup>-1</sup> , 5 mV s <sup>-1</sup> , 10 mV s <sup>-1</sup> , 20 mV s <sup>-1</sup> , and 50 mV s <sup>-1</sup> . ....	113
Figure 5-4 The specific capacitance of vanadium oxide nanoribbon in 2M KCl, 2M NaCl at the scan rates of 2 mV s <sup>-1</sup> , 5 mV s <sup>-1</sup> , 10 mV s <sup>-1</sup> , 20 mV s <sup>-1</sup> , 50 mV s <sup>-1</sup> . ....	114
Figure 6-1 Synthesis process of NiCo <sub>2</sub> O <sub>4</sub> @graphene nanoarchitectures: (A) a piece of PU-sponge and the solution with RGO stabilized using sodium cholate hydrate (SCH); (B) The RGO was coated and anchored onto the PU-sponge assisted by microwave and freeze drying; (C) NiCo <sub>2</sub> O <sub>4</sub> precursor nanosheets grown on RGO-PU-sponges; (D) 3D mesoporous hybrid NiCo <sub>2</sub> O <sub>4</sub> @graphene nanoarchitectures. (E) Crystallized NiCo <sub>2</sub> O <sub>4</sub> nanosheets with mesopores. ....	121
Figure 6-2 The SEM images of the (A, B) PU-sponge, showing macroporous structure; (C, D) RGO-PU-sponge, indicating RGO was coated onto PU-sponge. ....	122
Figure 6-3 SEM images of (A, B) NiCo <sub>2</sub> O <sub>4</sub> precursor sheets that grew on the skeleton of RGO-PU-sponge; (C) high magnification SEM image of NiCo <sub>2</sub> O <sub>4</sub> precursor with macropores. ....	123
Figure 6-4 (A) XRD pattern of NiCo <sub>2</sub> O <sub>4</sub> @graphene nanoarchitectures. (B) SEM image of foam-like hybrid NiCo <sub>2</sub> O <sub>4</sub> @graphene nanoarchitectures with hierarchical pores. (C)	

SEM image of NiCo <sub>2</sub> O <sub>4</sub> nanosheets.....	124
Figure 6-5 The SEM images of (A, B) large-size NiCo <sub>2</sub> O <sub>4</sub> @graphene obtained by annealing the precursor at 350 °C in air for 2 hours; TEM images of (C) NiCo <sub>2</sub> O <sub>4</sub> @graphene nanoarchitectures with macropores, (D) mesopores ranging from 2-5nm.	125
Figure 6-6 (A) TEM image of NiCo <sub>2</sub> O <sub>4</sub> @graphene nanosheets, showing the porous architecture. (B) HRTEM images of NiCo <sub>2</sub> O <sub>4</sub> @graphene nanosheets. The inset SAED pattern can be fully indexed to polycrystalline NiCo <sub>2</sub> O <sub>4</sub> . (C) Lattice resolved HRTEM image of NiCo <sub>2</sub> O <sub>4</sub> nanosheets.....	126
Figure 6-7 (A) Nitrogen adsorption/desorption isotherms; (B) pore size distribution of NiCo <sub>2</sub> O <sub>4</sub> @ graphene nanoarchitectures.....	127
Figure 6-8 Electrochemical performance of the NiCo <sub>2</sub> O <sub>4</sub> @graphene nanoarchitectures. (A) CV curves at the scan rate of 5 mV s <sup>-1</sup> to 200 mV s <sup>-1</sup> ; (B) constant-current charge/discharge profile at the current densities of 1 A g <sup>-1</sup> to 80 A g <sup>-1</sup> ; (C) specific capacitance vs current density; (D) capacity retention vs cycle number up to 10,000 cycles at 10 A g <sup>-1</sup> . All the data are taken in 2.0 M KOH electrolyte.....	128
Figure 6-9 Charging/discharging profile of pure Ni foam at the same current rates of the active material, ranging from 1 to 40 A g <sup>-1</sup> . .....	129
Figure 6-10 Electrochemical performance of NiCo <sub>2</sub> O <sub>4</sub> @graphene nanoarchitectures and bare NiCo <sub>2</sub> O <sub>4</sub> (A) charging/discharging curves at a current density of 10 A g <sup>-1</sup> ; (B) specific capacitances at current densities of 1 to 80 A g <sup>-1</sup> ; (C) capacities retention up to 10000 cycles at 10 A g <sup>-1</sup> ;.....	131
Figure 6-11 Nyquist plots of the a.c. impedance spectra of the porous NiCo <sub>2</sub> O <sub>4</sub> @graphene electrode and the bare NiCo <sub>2</sub> O <sub>4</sub> electrode in the frequency range from of 100 kHz to 0.01 Hz.....	132
Figure 7-1 Schematic illustration showing the experimental steps of fabricating	

NiCo <sub>2</sub> O <sub>4</sub> @graphene foam. ....	141
Figure 7-2 The schematics of the (a) upper base, (b) bottom base and (c) cylinder tube of the as-designed device. (d) The images of the device (left image), after inserting the plunger (right image). ....	142
Figure 7-3 The compression test shows that the as-prepared foam has a high-rigid mechanical property. The foam has (a) a diameter of 14 mm and (b) a thickness of about 2 mm. (c) The real-time image of the compressed sample loading with the balance of 100 g. (d) the images of the sample after loading the weights, shows that the foam retained the original structure without collapsing. (e) There is no change in the thickness of the foam after loading the related balance weight. ....	144
Figure 7-4 The real-time images of the compressed sample loading with the balance of (a) 2 g, (d) 10 g, (g) 20 g and (j) 50 g. (b), (e), (h) and (k) the images of the sample after loading these weights, showing the foam retained the original structure without collapsing. (c), (f), (i) and (l) there is no change in the thickness of the foam after loading the related balance weight.....	145
Figure 7-5 The compression test of the material fabricated without using extra air compress pressure. (a) The size of the foam is smaller than that of filter paper due to the shrink during the freeze drying process. (b) Cross-sectional image of the foam, showing cone-like structure. (c) The foam was loaded with the balance of 20g. (d) and (e) The image of sample after loading the weight, showing the foam suffered structure collapsing. ....	146
Figure 7-6 (a) SEM images of NiCo <sub>2</sub> O <sub>4</sub> precursor foam after freeze drying. (b) Magnified SEM image showing NiCo <sub>2</sub> O <sub>4</sub> precursor gown on GO sheets. ....	147
Figure 7-7 (a) XRD pattern of the NiCo <sub>2</sub> O <sub>4</sub> @graphene nanoarchitectures. (b) SEM images of the foam indicating a compressed structure with small-size pores, ranging from	

1-10 um. (c) The magnified SEM image of ROG sheets. (d) Cross-sectional SEM image of the foam which shows plenty of horizontal channels built by NiCo<sub>2</sub>O<sub>4</sub>@graphene sheets. (e) SEM image of the fully filtered NiCo<sub>2</sub>O<sub>4</sub>@graphene, indicating the NiCo<sub>2</sub>O<sub>4</sub>@graphene sheets stacked together without the porous structure and vertical channels. (f) SEM image of the 1 ml NiCo<sub>2</sub>O<sub>4</sub>@graphene precursor directly freeze dried without filtration, showing random structure and fragile property. .... 148

Figure 7-8 (a) Image of the material after annealing at 600 °C for 2 hours in pure argon and then 250 °C for 2 hours in air. (b) The SEM images of the foam with vertical channels with respect to the current collector. (c) Magnified SEM image of the foam showing the pore size from 1um to 10 um. (d) Magnified cross-sectional SEM images (Figure 3d) of the foam..... 149

Figure 7-9 (a) Low-magnified and (b) high-magnified SEM images of the fully filtered NiCo<sub>2</sub>O<sub>4</sub>@graphene. .... 150

Figure 7-10 (a) TEM image of the NiCo<sub>2</sub>O<sub>4</sub>@graphene nanosheets of the foam, showing uniform distribution of NiCo<sub>2</sub>O<sub>4</sub> on RGO sheet. (b) Magnified TEM image of the NiCo<sub>2</sub>O<sub>4</sub> nanoparticles, ranging from 20 - 50 nm. (c) HRTEM image of the NiCo<sub>2</sub>O<sub>4</sub> nanoparticle. The lattice spacing of 0.2 nm corresponds to the (4 0 0) lattice planes, the lattice spacing of 0.245 nm corresponds to the (3 1 1) lattice planes and the lattice spacing of 0.4 nm corresponds to the (2 0 0) lattice planes. The inset SAED pattern can be indexed to the diffraction planes of the spinel phase of NiCo<sub>2</sub>O<sub>4</sub>..... 151

Figure 7-11 Energy dispersive X-ray spectroscopy (EDS) characterization of the 3D free-standing NiCo<sub>2</sub>O<sub>4</sub>@graphene foam. (a) SEM image of part of the foam; (b) elemental mapping image of the foam; (c-f) EDS Ni, O, Co and C mapping of the region as show in (a). .... 152

Figure 7-12 EDS spectrum captured for the region shown in Figure 6-11 (a)..... 153

Figure 7-13 N<sub>2</sub> adsorption–desorption isotherms of the 3D NiCo<sub>2</sub>O<sub>4</sub>@graphene foam. The inset shows the pore size distribution. .... 153

Figure 7-14 Electrochemical performance of the NiCo<sub>2</sub>O<sub>4</sub>@graphene foam. (a) CV curves at a scan rate of 5 mV s<sup>-1</sup> to 200 mV s<sup>-1</sup>; (b) constant-current charge/discharge profile at current densities of 2 A g<sup>-1</sup> to 80 A g<sup>-1</sup>; (c) specific capacitance vs. current density; (d) capacity retention vs. cycle number up to 5000 cycles at 10 A g<sup>-1</sup>. All the data are taken in 2.0 M KOH electrolyte. .... 154

Figure 7-15 Electrochemical performance of 3D NiCo<sub>2</sub>O<sub>4</sub>@graphene foam and the fully filtered NiCo<sub>2</sub>O<sub>4</sub>@graphene (a) Charging/discharging curves at a current density of 10 A g<sup>-1</sup>; (b) Specific capacitances at current densities of 2 to 80 A g<sup>-1</sup>; (c) Capacities retention up to 5000 cycles at 10 A g<sup>-1</sup>..... 156

## LIST OF TABLES

Table 2-1 Comparison of the supercapacitor from different companies.....	14
Table 2-2 Comparison of different kind of batteries.....	15
Table 5-1 Comparison of the specific capacitance value of as-prepared vanadium oxide nanoribbon with the reported studies in different electrolyte at the scan rate of 5 mV s <sup>-1</sup> .....	115
Table 6-1 Comparison of the electrochemical performance of as-prepared NiCo <sub>2</sub> O <sub>4</sub> @graphene with the materials reported in the literatures .....	132

## **ABSTRACT**

Energy storage systems (ESSs) play a critical role in plenty of applications including renewable energy systems, power systems for electric vehicles (EVs) and hybrid electric vehicles (HEVs), and electrical power grids for improving reliability and overall use of the entire system. Currently, there are several types ESSs dominated the energy storage. Each kind of ESSs has their own operation mechanism, energy efficiency, energy density, power density, cycle life, charge and discharge capability, cost efficiency, operating temperature. The common ESS is based on lead acid battery which stores electrical energy in the form of chemical energy. However, if the batteries are overdischarged or kept at a discharged state, its capability will be irreversibly undermined because the sulfate crystals become larger and more difficult to break up during recharge. Since the first NiCd battery was created by Waldemar Jungner in 1899, even though NiCd battery technologies have experienced a series of evolutionary developments, its demerits are obvious including 1) shorter life cycle; 2) memory effect; 3) toxicity of Cd; 4) lower energy density; and 5) limited negative temperature coefficient. Based on the development of NiCd battery technology, nickel metal hydride (NiMH) batteries was proposed by researchers which possess better performance than NiCd batteries in cycle life, energy density and charge&discharge rates. Lithium ion is the preferred chemistry, having a superior specific energy and power density to nickel metal hydride. More lithium per gram stored in the electrodes contributes to higher energy density and power density. In addition to chemical battery system, researchers recently proposed some new sorts of ESSs including flywheel, compressed air energy storage (CAES), superconductive magnetic energy storage (SMES), etc. All of them can provide super energy density and power density. But they are more or less blocked ether in complex mechanical

construction or cooling device.

Supercapacitor has emerged to be an exciting energy storage device, which is able to provide high specific power, charge and discharge up to million times, have long lifetime and broad range of working temperature. Even though supercapacitor has been widely seen as a promising energy storage candidate to replace the traditional chemical batteries, it also suffer its drawback that the low energy density (the energy stored in per unit of volume and weight), high equivalent series resistance (ESR) and its high cost associated with its performance.

Therefore, this PHD thesis project aims to address these drawbacks of supercapacitor by designing different nanotechnologies and fabrication methods to synthesize advance materials with better performance than that of conventional supercapacitor. A Series of designed structures and materials were fabricated by designed methods. All the materials were also investigated by using X-ray diffraction, scanning electron microscopy (SEM), transmission electron microscopy (TEM) observation techniques, Brunauer–Emmett–Teller (BET) surface area measurement and electrochemical testing.

A facile and effective hydrothermal treatment that is able to control the condensation speeds of precursors in the solution along the  $\langle 010 \rangle$ ,  $\langle 100 \rangle$  and  $\langle 001 \rangle$  directions was designed to fabricate vanadium oxide nanoribbon used for the electrode of supercapacitor. It was achieved by controlling the hydrothermal reaction time and the weight ratio to synthesize the ultralong vanadium oxide nanoribbon with controlled width. It has high specific capacitance of  $453 \text{ F g}^{-1}$  at the scan rate of  $2 \text{ mV s}^{-1}$  in  $2 \text{ M NaCl}$  electrolyte, and it still maintained a high capacitance of  $201 \text{ F g}^{-1}$  at a higher scan rate of  $50 \text{ mV s}^{-1}$ , attributing to the easy ion insertion and electronic transport along the a-b plane rather through the layers of the c-axis.



Vanadium oxide nanotubes were synthesized by a revised hydrothermal treatment with high-speed stirring. The preparation involved dissolution of  $V_2O_5$  into  $H_2O_2$  and high-speed stirring (10000 r/min) with hexadecylamine. The product was characterized by scanning electron microscopy, transmission electron microscope, X-ray diffraction and thermogravimetric analysis. The electrochemical properties of the materials as electrodes for electrochemical capacitors were evaluated by cyclic voltammetry in a three electrode system consisting of a saturated calomel electrode as reference electrode, platinum as a counter electrode and the active materials as the working electrode. A high capacitance of  $148.5 \text{ F g}^{-1}$  was obtained at a scan rate of  $2 \text{ mV s}^{-1}$  in 2M KCl. The electrode maintained a high capacitance of  $105 \text{ F g}^{-1}$  at a higher scan rate of  $50 \text{ mV s}^{-1}$  in 2M KCl electrolyte.

3D mesoporous hybrid  $NiCo_2O_4@graphene$  nanoarchitectures were successfully synthesized by a combination of freeze drying and hydrothermal reaction. Field-emission scanning electron microscopy (FESEM) and TEM analyses revealed that  $NiCo_2O_4@graphene$  nanostructures consist of a hierarchical mesoporous sheet-on-sheet nanoarchitecture with a high specific surface area of  $194 \text{ m}^2 \text{ g}^{-1}$ . Ultrathin  $NiCo_2O_4$  nanosheets, with a thickness of a few nanometers and mesopores ranging from 2 to 5 nm, were wrapped in graphene nanosheets and formed hybrid nanoarchitectures. When applied as electrode materials in supercapacitors, hybrid  $NiCo_2O_4@graphene$  nanosheets exhibited a high capacitance of  $778 \text{ F g}^{-1}$  at the current density of  $1 \text{ A g}^{-1}$ , and an excellent cycling performance extending to 10000 cycles at the high current density of  $10 \text{ A g}^{-1}$ .

We also presented a rational, large-scale and general method, called controllable freeze casting (CFC), to fabricate a high-densely assembled and aligned free-standing  $NiCo_2O_4@graphene$  3D foam by vacuum filtration and air compress pressure assembly method. In the designed method, the amount of water is controllable, therefore controlling

the size and the shape of the ice when the material was introduced into freeze drying system, finally achieving controllable pore size and aligned structure. This free-standing foam retains the intrinsic properties of graphene sheet, such as high surface area and high electrical conductivity. In the foam, the graphene sheets build the high conductive skeletons. And the skeletons with high surface areas support the uniform distribution of NiCo<sub>2</sub>O<sub>4</sub> nanoparticles on the graphene sheets. By controlling the amount of water in the precursor, it is possible to fabricate 3D NiCo<sub>2</sub>O<sub>4</sub>@graphene foams with a wide range of thickness and pore size. This dense NiCo<sub>2</sub>O<sub>4</sub>@graphene material exhibited a high capacitance of 790 F g<sup>-1</sup> at a current density of 2 A g<sup>-1</sup>, and an excellent cycling performance at a high current density of 10 A g<sup>-1</sup>. The compression test revealed that the 3D NiCo<sub>2</sub>O<sub>4</sub>@graphene foam exhibited strong mechanical property which is able to support 20,000 times its own weight without structure collapsing. The novel synthesis method of such 3D foam with excellent properties paves the way to explore the application of lamellar materials like graphene in a self-supporting, metal oxide deposition and 3D foam.